Evaluation of an Anatomical Based MAP Reconstruction Algorithm for PET in Epilepsy

Kristof Baete, *Student Member, IEEE,* Johan Nuyts, *Member, IEEE,* Wim Van Paesschen, Paul Suetens, *Member, IEEE,* and Patrick Dupont

***Abstract*— We studied the performance of an anatomical based maximum-a-posteriori reconstruction algorithm (A-MAP) for the detection of hypo-metabolic regions in positron emission tomography (PET) of the brain of epilepsy patients. Between seizures, 2-[^{18}F]fluoro-2-deoxy-D-glucose PET shows a decreased glucose metabolism in gray matter (GM) associated with the epileptogenic region. However, detection of these regions is limited by noise in the measurement and the relatively small thickness of GM compared to the spatial resolution of PET. We hypothesized that incorporating anatomical information, derived from magnetic resonance imaging data, and pathophysiological knowledge in the reconstruction process improves the detection of hypo-metabolic regions. Monte-Carlo based brain software phantom experiments were used to examine the performance of A-MAP. The influence of small misregistration errors of the anatomical information and weight of the a priori information in GM were studied. A-MAP showed improved results for signal-to-noise ratio, bias and variance. A human observer study was performed, showing improved detection of hypo-metabolic regions using A-MAP compared to maximum-likelihood (ML) reconstruction. Finally, A-MAP was applied to clinical PET data of an epilepsy patient. We can conclude that the use of anatomical and pathophysiological information during the reconstruction process is promising for the detection of subtle hypo-metabolic regions in the brain of patients with epilepsy.**

I. Introduction

IT is known that epileptic seizures are the result of abnormal discharges of a group nerve cells in specific areas in the gray matter (GM) tissue of the human brain [1]. Surgical removal of the epileptogenic region, i.e. the region that includes the lesion which is causing the epileptic seizures, can cure patients with refractory partial epilepsy. Positron emission tomography (PET) of the cerebral glucose metabolism between seizures, using 2-[^{18}F]fluoro-2-deoxy-D-glucose (FDG), has shown to be useful in the process of presurgical evaluation [2], [3]. In fact, FDG-PET can replace more invasive diagnostic procedures, such as e.g. the surgical insertion of depth electrodes into deep brain structures [4]. Between seizures, FDG-PET of the brain of patients with refractory partial epilepsy often shows a decreased glucose metabolism in certain areas of the GM. Usually, these hypo-metabolic regions are associated with the epileptogenic region. Unfortunately, these hypo-metabolic regions can be very subtle and difficult to detect. Moreover, the image quality can have a serious influence on the detection task.

The image quality of PET is affected by noise, caused by a variety of physical effects (e.g. the radioactive decay, scan duration, the amount of administered radiopharmaceutical). However, an important issue when imaging the human brain using emission computed tomography remains to be the limited spatial resolution of the system. The brain exhibits a complex anatomical structure in which the GM thickness can have relatively small spatial dimensions compared to the resolution of the PET system (about 3 mm, [5]). Furthermore, there can be a large variation in thickness and geometry of several of the brain substructures. This might cause an underestimation of the tracer activity in the reconstructed image [6]. This effect, called the partial volume effect (PVE), can lead to spurious hypo-metabolic regions. In the presurgical evaluation of epilepsy, this can result in an increase of false positive predicted hypo-metabolic regions. Moreover, if the finite spatial resolution of the imaging system is not accounted for, spill over of activity to neighboring regions can occur. This can yield a possible misinterpretation of the extent of hypo-metabolic regions. Thereby, presurgical delineation of these regions becomes difficult and less accurate.

We hypothesize that the use of anatomical information, derived from magnetic resonance imaging (MRI) data, and the pathophysiological knowledge of epilepsy during the reconstruction process improves the detection of hypo-metabolic regions. For that purpose, an anatomical based maximum-a-posteriori reconstruction algorithm (A-MAP) was developed [7]. In this study, we make an evaluation of this iterative reconstruction algorithm.

II. Methods

If no lesions or tumors are present, one can reasonably assume that for FDG-PET the metabolic activity of the white matter (WM) tissue is much lower and much more uniform than in the GM tissue [8], [9]. Moreover, no tracer accumulation is expected in the cerebrospinal fluid (CSF) during the measurement. The identification of GM, WM and CSF can be obtained from high-resolution MRI of the brain. We assume that the MRI data is normal. Current brain segmentation algorithms [10] can then very accurately determine these three tissue classes. In most segmentation algorithms, the procedure returns the probability that a voxel belongs to a certain tissue

Work supported by K.U.Leuven grants IDO-99/005, OT-00/32 and F.W.O. grant G.0174.03.

K. Baete, J. Nuyts and P. Dupont are with Nuclear Medicine, W. Van Paesschen is with Neurology, and P. Suetens is with Medical Image Computing, Radiology-ESAT/PSI, Katholieke Universiteit Leuven, B-3000 Leuven, Belgium. (e-mail: kristof.baete@uz.kuleuven.ac.be)

class. This is generally called a fuzzy tissue classification. For each voxel, we will assume that the probability for a tissue class approximates the underlying tissue composition. This implies that the segmentation probability is interpreted as a tissue fraction [11]. The set of segmentation images is then denoted $\{f^G, f^W, f^C, f^O\}$, with O for the class "other". This set represents the a priori anatomical knowledge which will be incorporated in the reconstruction algorithm. Using a state-of-the-art image registration algorithm [12], one can compute the affine transformation needed to align the MR image with the PET image. The reconstruction algorithm assumes perfect registration. However, we assess the influence of small misalignments in the evaluation experiments.

For a distribution of activity $\Lambda = \{\lambda_j \,|\, j \in \mathbb{J}\}$ in the field of view of a PET scanner, y_i photon pairs are measured at a line of response i. If λ_j represents the amount of activity at voxel j and c_{ij} is the probability that photons emitted in voxel j are detected in detector pair i, then the expected amount of photon pairs is $E(y_i) = \sum_j c_{ij}\lambda_j$. The matrix of detection probabilities $\{c_{ij}\}$, called the system matrix, contains a mathematical description of the projection process with the associated physical effects that take place between emission and detection of both photons. We assume that the measurements are samples from a Poisson distribution. Photon attenuation and (position independent) finite detector resolution are included in the system matrix. We will ignore scatter and randoms.

We define subsets of the complete set of voxels in image space $\mathbb{J}$. The subdivision is based on the anatomical information that is contained in the segmentation images of the aligned MRI data. We start with combining all voxels belonging to the "brain" into one subset, denoted $\mathbb{B}$,

$$\mathbb{B} = \{j \in \mathbb{J} \,|\, \left(f_j^G + f_j^W + f_j^C\right) > 0.01\}$$

The threshold value is chosen to be very small. This is to ensure that all voxels containing at least 1 % of GM, WM or CSF are included in subset "brain". In the class "brain" we make a subset of voxels containing at least partially GM, denoted $\mathbb{G}$,

$$\mathbb{G} = \{j \in \mathbb{B} \,|\, f_j^G > 0.01\}$$

The threshold value controls the inclusion of voxels containing partially GM in $\mathbb{G}$. Because the GM tissue has our special attention in epilepsy, we want that threshold value to be very small. Finally, within $\mathbb{B} \setminus \mathbb{G}$ we construct two subsets:

$$\mathbb{W} = \{j \in \mathbb{B} \setminus \mathbb{G} \,|\, f_j^W > 0.99\} \quad (1)$$

$$\mathbb{C} = \{j \in \mathbb{B} \setminus \mathbb{G} \,|\, f_j^C > 0.99\} \quad (2)$$

We want voxels composed of mainly WM to be included in $\mathbb{W}$ and voxels composed of mainly CSF to be included in subset $\mathbb{C}$. Therefore, the threshold values are set very high.

Every voxel j in the PET image space can be thought of as a source with an amount of activity λ_j equal to the sum of fractional activities of the contributing tissues, or

$$\lambda_j = f_j^G\lambda_j^G + f_j^W\lambda_j^W + f_j^C\lambda_j^C + f_j^O\lambda_j^O \quad (3)$$

If we can assume that the activity distribution inside WM and CSF is approximately uniform, we can as well replace the activity of these tissues inside region $\mathbb{G}$ with their mean activities, $\bar{\lambda}^W$ and $\bar{\lambda}^C$, calculated in regions $\mathbb{W}$ and $\mathbb{C}$, respectively. Furthermore, since the GM tissue is surrounded by WM or CSF, this implies that $\forall j \in \mathbb{G} : f_j^O \approx 0$. Thus, $\forall j \in \mathbb{G}$, we can approximate (3) with

$$\lambda_j \approx f_j^G\lambda_j^G + f_j^W\bar{\lambda}^W + f_j^C\bar{\lambda}^C \quad (4)$$

Instead of estimating $\Lambda = \{\lambda_j \,|\, j \in \mathbb{J}\}$, we can then compute the MAP estimator of Λ^*, with

$$\Lambda^* = \{\lambda_j^* \,|\, j \in \mathbb{J}\} = \{\lambda_j^G \,|\, j \in \mathbb{G}\} \cup \{\lambda_j \,|\, j \in \mathbb{J} \setminus \mathbb{G}\} \quad (5)$$

such that $E(y_i) = \sum_j c_{ij}^*\lambda_j^*$ with system matrix c_{ij}^* [7]. The propagation of noise in $\mathbb{W}$ and $\mathbb{C}$ is controlled using a Gaussian prior. In $\mathbb{G}$, we use a Gibbs smoothing prior designed to penalize relative differences between neighboring λ_j^G [13]. Finally, the MAP estimation of Λ^* is converted to Λ using the inverse parameter transformation, as explained in [7]. This means that for all $j \in \mathbb{G}$, λ_j^G has to be replaced by

$$f_j^G\lambda_j^G + f_j^W\bar{\lambda}^W + f_j^C\bar{\lambda}^C \quad (6)$$

This iterative reconstruction algorithm is called Anatomical based MAP (A-MAP).

III. Experiments

A. Simulation study

We studied the performance of the A-MAP versus the maximum-likelihood (ML) reconstruction algorithm for the detection of hypo-metabolic regions in FDG-PET data using Monte Carlo simulation experiments. The weight of the a priori anatomical information in the GM class $\mathbb{G}$ was investigated, as well as influences of small misalignments between the anatomical information and the emission data.

Since the human brain has a very unique and complex shape, we constructed a clinically realistic three-dimensional (3-D) baseline software phantom. The construction of the phantom was based on 30 consecutive trans-axial slices of the digital phantom provided by the *BrainWeb* database [14]. The matrix dimensions of the phantom are 218×218×30 voxels with an isotropic voxel size of 1 mm. GM, WM and CSF tissues were identified in the "discrete" anatomical model [15]. A baseline FDG-PET tracer distribution representing the glucose metabolism of a normal brain was constructed. Activity was set to 12.5 counts per voxel (cpv) in GM, 3.125 cpv in WM and 0 cpv in CSF. In a duplicate of the baseline phantom, called the hypo-metabolic phantom, activity in four 3-D regions within the GM was decreased by 25 % (see Table I).

The PET data acquisition process of a clinical PET scanner was simulated by projecting the baseline and the hypo-metabolic phantoms over 144 angles using a uniform attenuation image derived from the contour of the digital brain phantom. Projections were smoothed along the detector grid using a two-dimensional (2-D) Gaussian kernel with 5 mm full-width at half-maximum (FWHM). Thereby we account for the detector

resolution of the PET camera. The projections were resampled to 2×2 mm^2 detectors. Of each sinogram, 100 Poisson noise realizations were computed and reconstructed using the ML reconstruction algorithm. All reconstruction images were post-smoothed using a variety of 3-D Gaussian smoothing kernels with FWHM varying from 4 to 8 mm. The ML reconstructed images post-smoothed with 4 mm FWHM were used as the initial image for the A-MAP iterative reconstruction algorithm. We have used attenuation correction and resolution recovery in the reconstruction process of both ML and A-MAP.

The A-MAP reconstructions were performed using GM, WM and CSF "fuzzy" tissue classifications provided by the *BrainWeb* database [15]. The segmentation images were resampled to the PET grid. Dimensions are $109\times109\times15$ voxels with an isotropic voxel size of 2 mm. The emission data and anatomical information are by these means perfectly aligned. Three different weights of the Gibbs smoothing prior in $\mathbb{G}$ (A-MAP-1, 2, and 3) were used. Thereafter, the A-MAP-2 reconstructions were performed using intentionally misaligned anatomical information. Therefore, the tissue classification from the high-resolution MR data was (a) trans-axially shifted over 1 mm, and (b) rotated over 1 degree. Thereafter, the anatomical information was resampled to the PET grid.

We measured signal-to-noise ratio (SNR) [16] in regions-of-interest (ROI) around the four hypo-metabolic regions and the overall root mean squared (rms) bias and rms standard deviation for the reconstructions based on the baseline phantom.

B. Human observer study

We constructed a two-dimensional (2-D) realistic brain software phantom based on a trans-axial slice of the digital *BrainWeb* phantom [14]. Coordinates are $z = 8$ mm in the stereo-tactical Talairach framework [17]. Matrix dimensions are 218×218 voxels with an isotropic voxel size of 1 mm. The GM, WM and CSF tissues were identified in the "discrete" anatomical model [15] and a baseline phantom was constructed. Throughout the brain, we delineated 25 candidate hypo-metabolic regions restricted to the GM tissue. For 20 metabolic reduction values, proportionally ranging from 5 % to 100 % (stepsize 5%), and for each of the 25 regions, we constructed a hypo-metabolic phantom image. Thereby, each phantom contained one hypo-metabolic region with a specific hypo-metabolic reduction value (or lesion contrast value). All phantoms were resampled to a realistic PET grid of 109×109 voxels and an isotropic voxel size of 2 mm. The baseline activity was set to 100 counts per voxel (cpv) in GM, 25 cpv in WM and 0 cpv in CSF.

The PET data acquisition process of a clinical PET scanner was simulated by projecting all phantoms over 144 angles using uniform attenuation. The projections were smoothed using a two-dimensional (2-D) Gaussian with 5 mm full-width at half-maximum (FWHM) to account for the detector resolution. Poisson noise was added to the projection data and reconstructed using the ML algorithm. We have used attenuation correction and resolution recovery. It was left to the observer to control the amount of post-smoothing required for the observation of the ML reconstruction images.

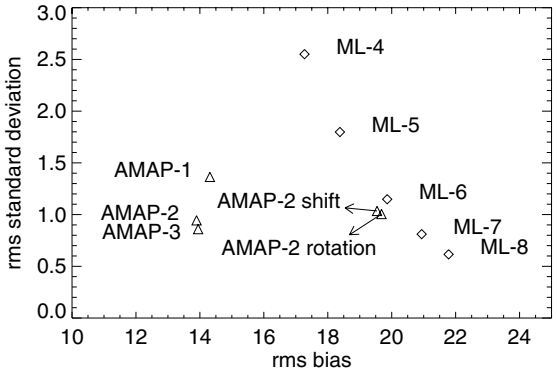

Fig. 1. Root mean squared (rms) bias and rms standard deviation results of the baseline phantom simulations. ML-X means post-smoothed ML using a 3-D Gaussian kernel with X mm FWHM.

A clinically realistic high-resolution noisy MR image, corresponding to the digital *BrainWeb* phantom, was requested from the *BrainWeb* MR simulator [14]. The noisy MR image was segmented into GM, WM and CSF tissues using the Statistical Parametric Mapping (SPM99) software package [18]. The fuzzy tissue segmentations were resampled to the PET grid and used in an A-MAP reconstruction of all simulated PET projection data of the baseline and hypo-metabolic phantoms.

An interactive computer program was written as a user interface for the human observers in order to evaluate the performance of detecting and localizing the induced hypo-metabolic regions. The user interface was based on in-house developed medical image viewing software that is also used in the daily clinical environment. Physicians were invited to carry out two separate observing sessions, one for images reconstructed using the A-MAP and one using the ML algorithm.

As an introduction to the observers, the program presented the reconstruction images of noise realizations of the baseline phantom. Thereby, observers were asked to get acquainted with the image quality, the influence of noise and the display settings. The observer was able to adjust the width of a 2-D Gaussian smoothing kernel applied during the image displaying. Selection of the color table, intensity scaling and zooming was adjustable. After the introduction, the program presented the reconstruction images of the hypo-metabolic phantom data in an order of decreasing hypo-metabolic reduction. For each of the 20 hypo-metabolic reduction values (or contrasts), the program selected and displayed consecutively, without repetitions, randomly 10 out of the 25 hypo-metabolic reconstruction images belonging to that reduction value.

The task of the observer was then to specify the most likely position of the hypo-metabolic region using a mouse click. Thus, we have designed a "multiple alternative forced choice" experiment [19]. If the indicated position was within 5 mm of the barycenter of the induced hypo-metabolic region, localization was considered to be correct. After every 10

TABLE I

RESULTS OF THE MONTE-CARLO SIMULATION EXPERIMENT. SIZE AND LOCATION OF THE HYPO-METABOLIC REGIONS AND SNR IN ROI AROUND THE FOUR HYPO-METABOLIC REGIONS. ML-X MEANS POST-SMOOTHED ML USING A 3-D GAUSSIAN KERNEL WITH X MM FWHM.

Hypo-metabolic region	1	2	3	4
Size (cm^3)	1.5	1.2	0.8	1.7
Location	frontal	parietal	temporal	occipital
SNR				
Reconstruction algorithm	ROI 1	ROI 2	ROI 3	ROI 4
ML-4	38.0	31.5	21.1	39.5
ML-5	41.6	33.4	23.0	42.6
ML-6	45.5	35.4	25.2	45.3
ML-7	47.7	36.6	26.6	46.6
ML-8	48.9	37.5	27.4	47.2
A-MAP-1	42.3	37.6	23.9	40.8
A-MAP-2	44.9	37.8	23.5	41.0
A-MAP-3	45.4	36.9	23.2	41.2
A-MAP-2 (1 mm shift)	45.9	38.9	23.3	41.7
A-MAP-2 (1 deg rotation)	45.7	38.2	23.8	42.3

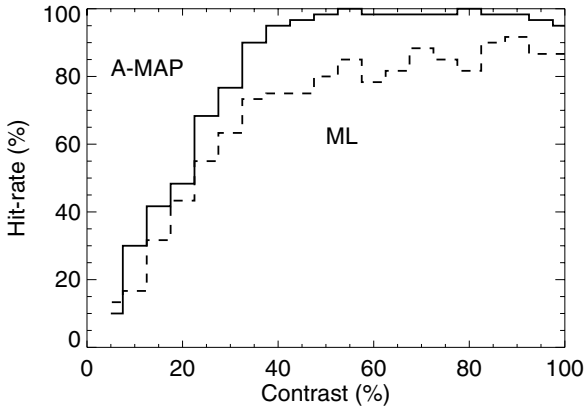

Fig. 2. The average correct hit-rate over all observers versus the contrast of the hypo-metabolic regions for the ML and the A-MAP algorithms. The dashed lines are the results of the observers who started with the ML session followed by the A-MAP session. The solid lines are the results of the observers who started with the A-MAP session followed by the ML session.

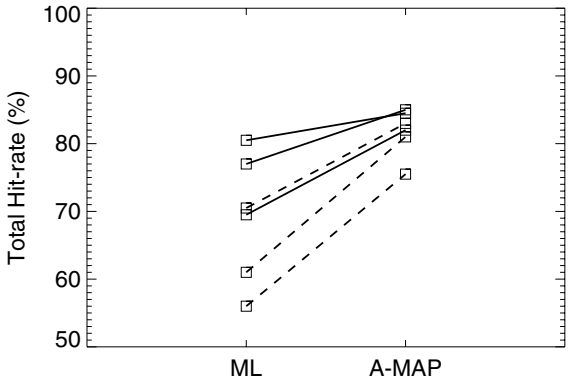

Fig. 3. The total correct hit-rate per observer for the ML and the A-MAP reconstruction algorithm over all contrasts. Dashed lines are for the three observers who started with the ML session. Solid lines are for the three observers who started with the A-MAP session.

images, the observer received feedback about the number of correct localizations. Presentation of all reconstruction images was accompanied by the noisy MR image, from which the anatomical data was derived. This image served as additional anatomical information for both ML and A-MAP reconstruction images. Where the program was used for observing A-MAP reconstruction images, both the final reconstruction image Λ as well as the MAP estimated reconstruction image Λ^* were shown. It was explained to the observers what the reconstruction images represented. We asked one half of the observers to complete first the observation session for the ML algorithm and then start with the observation session of the A-MAP algorithm. The other half were asked to do that the other way. We measured the mean correct hit-rate versus contrast over all observers and the total correct hit-rate per observer for ML and A-MAP. A Paired t-Test was applied to determine if the average difference between the total correct hit-rate of ML and A-MAP was essentially zero or not.

C. Patient study

We selected PET and MRI data of an epilepsy patient for which video electro-encephalography (EEG) during and between seizures showed left anterotemporal epileptic EEG patterns. The MRI data of that patient showed no lesions or structural abnormalities. The measurements were performed in 3-D mode with a SIEMENS-CTI ECAT EXACT HR+ scanner. The emission data were pre-corrected for randoms and scatter. The Fourier rebinning (FORE) algorithm was then applied to the 3-D emission data [20]. A transmission scan was taken to correct for attenuation. Resolution recovery was used during the reconstruction process of both A-MAP and ML. The ML reconstruction was post-smoothed using a Gaussian kernel with 5 mm FWHM. The anatomical information used in the A-MAP reconstruction was based on a T1-weighted MR scan of the patient. Segmentation of the GM, WM and CSF tissues was performed using SPM99 [18]. The patient underwent left temporal lobe resection (including the amygdala but not the hippocampus). The patient is free of seizures since surgery (2 years).

IV. RESULTS

A. Simulation study

Fig. 1 shows the rms bias and rms standard deviation results of the simulation study. A-MAP shows a reduction of bias compared to post-smoothed ML. Variation of the prior weight in $\mathbb{G}$ has more effect on standard deviation than on bias. Small mis-registrations have more effect on bias than on standard deviation. The SNR results are shown in Table I. A-MAP shows slight improved SNR results, compared to moderately post-smoothed ML. A-MAP shows some robustness for small mis-registrations and for the prior weight in $\mathbb{G}$.

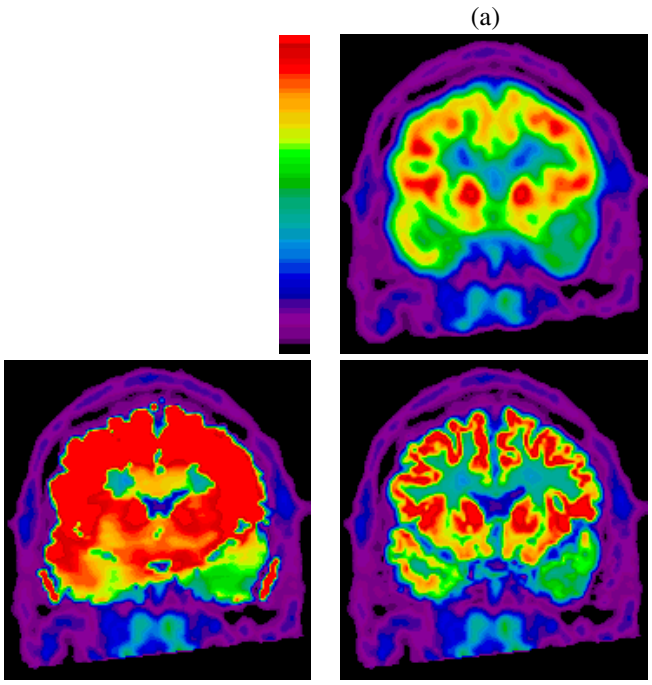

Fig. 4. Coronal view of the clinical PET data of an epilepsy patient reconstructed using (a) post-smoothed ML using a 3-D Gaussian kernel with $5ud$ mm FWHM, (b) the MAP estimation of Λ^* and (c) the final A-MAP reconstruction image Λ.

B. Human observer study

Six nuclear medicine physicians participated in the human observer study. Three of the observers started with the ML session, the other three started with the A-MAP session. The mean diameter of the hypo-metabolic regions was 11 voxels and the mean size was 94 voxels (2×2 mm^2 voxels). Fig. 2 shows the mean correct hit-rate over all observers versus the contrast of the hypo-metabolic regions for the ML and the A-MAP algorithms. Fig. 3 shows the total correct hit-rate per observer for ML and A-MAP over all contrasts. The Paired t-Test showed $p < 0.004$, meaning that the total correct hit-rate of A-MAP is significantly higher than that of ML. The total correct hit-rate of ML shows to have a larger variance than that of A-MAP. The total correct hit-rate of the observers who started with the ML session (dashed lines) show to be somewhat lower than the results of the observers who started with the A-MAP session (solid lines), indicating a possible learning effect.

C. Patient study

Fig. 4 shows promising results of the A-MAP reconstruction algorithm compared to post-smoothed ML when using clinical PET data.

V. Conclusion

Anatomical based MAP reconstruction of FDG-PET data shows to be promising for the detection of subtle hypo-metabolic regions in the brain of patients with refractory partial epilepsy. Further simulations and clinical evaluation is needed.

References

[1] G.L. Westbrook, "Seizures and epilepsy" in *Principles of neural science*, 4th ed., E.R. Kandel, J.H. Schwartz, and T.M. Jessell, Eds. New York, NY: McGraw-Hill, 2000, pp. 910–935.

[2] F. Rosenow and H. Lüders, "Presurgical evaluation of epilepsy," *Brain*, vol. 124, no. 9, pp. 1683–1700, Sep. 2001.

[3] S. Asenbaum and C. Baumgartner, "Nuclear medicine in the preoperative evaluation of epilepsy," *Nucl. Med. Commun.*, vol. 21, pp. 835–840, Jul. 2001.

[4] W.H. Theodore, S. Sato, C.V. Kufta, W.D. Gaillard, and K. Kelley, "FDG-positron emission tomography and invasive EEG: seizure focus detection and surgical outcome," *Epilepsia*, vol. 38, no. 1, pp. 81–86, Jan. 1997.

[5] B. Fischl and A.M. Dale, "Measuring the thickness of the human cerebral cortex from magnetic resonance images," *Proc. Natl. Acad. Sci. USA*, 2000, vol. 97, no. 20, pp. 11050–11055.

[6] F. Fazio and D. Perani, "Importance of partial-volume correction in brain PET studies," *J. Nucl. Med.*, vol. 41, no. 11, pp. 1849–1850, Nov. 2000.

[7] K. Baete, J. Nuyts, W. Van Paesschen, P. Suetens, and P. Dupont, "Detection of epileptogenic regions in FDG-PET using anatomical information," *Proc. IEEE Nuc. Sci. Symp. and Med. Imag. Conf.*, M10-94, Norfolk, VA, USA, Nov. 2002.

[8] S.C. Huang, M.E. Phelps, E.J. Hoffman, K. Sideris, C.J. Selin, and D.E. Kuhl, "Noninvasive determination of local cerebral metabolic rate of glucose in man," *Am. J. Physiol.*, vol. 238, pp. E69–E82, 1980.

[9] F. Turkheimer, R.M. Moresco, G. Lucignani, L. Sokoloff, F. Fazio, and K. Schmidt, "The use of spectral analysis to determine regional cerebral glucose utilization with positron emission tomography and [^{18}F]-fluorodeoxyglucose: theory, implementation, and optimization procedures," *J. Cereb. Blood Flow Metab.*, vol. 14, no. 3, pp. 406–422, 1994.

[10] K. Van Leemput, F. Maes, D. Vandermeulen, and P. Suetens, " Automated model-based tissue classification of MR images of the brain," *IEEE Trans. Med. Imag.*, vol. 18, no. 10, pp. 897–908, Oct. 1999.

[11] S. Sastry, and R.E. Carson, "Multimodality Bayesian algorithm for image reconstruction in positron emission tomography: a tissue composition model," *IEEE Trans. Med. Imag.*, vol. 16, no. 6, pp. 750–761, Dec. 1997.

[12] F. Maes, A. Collignon, D. Vandermeulen, G. Marchal and P. Suetens, "Multimodality image registration by maximization of mutual information," *IEEE Trans. Med. Imag.*, 1997, vol.16, no. 2, pp. 187–198.

[13] J. Nuyts, D. Bequé, P. Dupont and L. Mortelmans, "A concave prior penalizing relative differences for maximum-a-posteriori reconstruction in emission tomography," *IEEE Trans. Nucl. Sc.*, vol. 49, no. 1, pp. 56–60, Feb. 2002.

[14] (2002) BrainWeb. [Online]. Available: www.bic.mni.mcgill.ca/brainweb/

[15] D.L. Collins, A.P. Zijdenbos, V. Kollokian, J.G. Sled, N.J. Kabani, C.J. Holmes, and A.C. Evans, "Design and construction of a realistic digital brain phantom," *IEEE Trans. Med. Imag.*, vol. 17, no. 3, pp. 463–468, Jun. 1998.

[16] H.H. Barrett, J. Yao, J.P. Rolland, and K.J. Myers, "Model observers for assessment of image quality," *Proc. Natl. Acad. Sci. USA*, vol. 90, no. 21, pp. 9758–9765, Nov. 1993.

[17] J. Talairach and P. Tournoux, "Co-planar stereotaxic atlas of the human brain," Thieme, New York, 1988.

[18] (2003) SPM. [Online]. Available: www.fil.ion.ucl.ac.uk/spm

[19] A.E. Burgess, "Comparison of receiver operating characteristic and forced choice observer performance measurement methods," *Med. Phys.*, vol. 22, no. 5, pp. 643–655, May 1995.

[20] M. Defrise, "A factorization method for the 3D X-ray transform," *Inverse Problems*, vol. 11, no. 5, pp. 983–994, 1995.